

# Understanding Thermal Drift in Liquid Nitrogen Loads Used for Radiometric Calibration in the Field

SCOTT N. PAINE

*Smithsonian Astrophysical Observatory, Cambridge, Massachusetts*

DAVID D. TURNER

*NOAA/National Severe Storms Laboratory, Norman, Oklahoma*

NILS KÜCHLER

*Institut für Geophysik und Meteorologie, Universität zu Köln, Cologne, Germany*

(Manuscript received 20 August 2013, in final form 17 December 2013)

## ABSTRACT

An absorbing load in a liquid nitrogen bath is commonly used as a radiance standard for calibrating radiometers operating at microwave to infrared wavelengths. It is generally assumed that the physical temperature of the load is stable and equal to the boiling point temperature of pure N<sub>2</sub> at the ambient atmospheric pressure. However, this assumption will fail to hold when air movement, as encountered in outdoor environments, allows O<sub>2</sub> gas to condense into the bath. Under typical conditions, initial boiling point drift rates of order 25 mK min<sup>-1</sup> can occur, and the boiling point of a bath maintained by repeated refilling with pure N<sub>2</sub> can eventually shift by approximately 2 K. Laboratory bench tests of a liquid nitrogen bath under simulated wind conditions are presented together with an example of an outdoor radiometer calibration that demonstrates the effect, and the physical processes involved are explained in detail. A key finding is that in windy conditions, changes in O<sub>2</sub> volume fraction are related accurately to fractional changes in bath volume due to boiloff, independent of wind speed. This relation can be exploited to ensure that calibration errors due to O<sub>2</sub> contamination remain within predictable bounds.

## 1. Introduction

The absolute calibration of radiometers used to measure thermal radiation from the atmosphere is typically performed using two black absorbing loads serving as radiance standards, one maintained near ambient temperature  $T_{\text{amb}} \approx 290$  K and one cooled by immersion in a liquid nitrogen (LN2) bath to  $T_{\text{bath}} \approx 77$  K (Hardy 1973; Penzias and Burrus 1973). One advantage of this method is that this range of calibration temperatures roughly spans the range of brightness temperatures in the atmospheric scene. Another is that the load temperatures are relatively easy to characterize accurately. In the ambient load, the absence of significant temperature gradients to the environment enables accurate thermometry

of the absorber. In the cold load, immersion contact with the LN2 bath maintains the absorber uniformly at the bath temperature.

It is generally assumed that the LN2 bath temperature is equal to the boiling point of pure N<sub>2</sub> at ambient pressure, but this holds strictly only if the liquid is in contact with pure N<sub>2</sub> at the liquid–gas interface. This condition is always met, at least initially, for the internal interfaces at bubbles within the bath. In laboratory environments with little air movement, it is also met to good approximation at the upper surface of the bath because the bath surface develops a covering blanket of N<sub>2</sub> boiloff gas. This covering layer is often made evident by a thin, stable layer of water fog lying above the clear gas in contact with the bath.

Radiometers operated in the field, however, are usually calibrated under conditions in which air at ambient temperature having atmospheric composition is continuously brought into contact with the LN2 bath surface.

---

*Corresponding author address:* Scott Paine, Smithsonian Astrophysical Observatory, 60 Garden St., MS 78, Cambridge, MA 02138.  
E-mail: spaine@cfa.harvard.edu

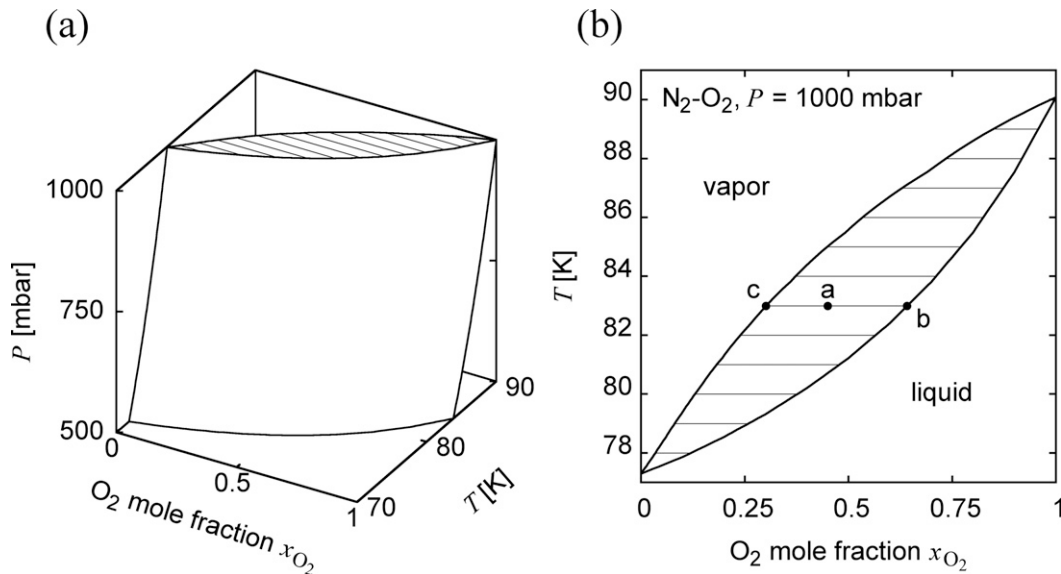


FIG. 1. (a) As a function of the state variables  $P$ ,  $T$ , and  $x_{O_2}$  and (b) at constant pressure  $P = 1000$  mbar.

This is because even a light wind is sufficient to displace the boiloff gas. Under these conditions, condensable atmospheric constituents, including  $O_2$ ,  $H_2O$ , and Ar, will collect in the bath. A goal of this study was to determine the rate and magnitude of the changes in bath temperature due to the uptake of contaminants under controlled laboratory conditions modeling conditions encountered in the field. We find that the bath temperature can be understood by treating the bath as a  $N_2$ – $O_2$  mixture without considering other contaminants. Nevertheless, as discussed below, the properties of the water ice that accumulates in the bath are also of interest and serve to clarify the physical picture of the processes taking place at the bath surface.

A second effect that can lead to calibration error is the reflection at the LN2 surface. For broadband radiometers with multimode detectors, such as Fourier transform spectrometers with bolometric detectors, the reflection can be accurately accounted for by considering the power reflection coefficient at the LN2 surface and the termination temperature of the reflected optical path as, for example, in Paine and Turner (2013). For narrowband radiometers based on microwave or millimeter-wave receivers with single-mode detectors, reflections can lead to coherent interference effects that are more complex (Randa et al. 2005). In particular, if a standing wave is formed between the radiometer and the LN2 surface, then the apparent load temperature will vary with changes in the surface height of the LN2 as it boils off (Küchler 2012; Pospichal et al. 2012).

This paper is organized as follows. We begin with a brief review of liquid–vapor equilibrium for  $N_2$ – $O_2$

mixtures in section 2. In section 3 we describe laboratory measurements of bath temperature as a function of time and boiloff fraction for varying simulated wind speeds across the liquid surface, and measurements of the steady-state temperature cycle of a bath periodically refilled with pure LN2. A key finding is that changes in  $O_2$  volume fraction, and hence bath temperature, are related accurately to the fractional changes in bath volume due to boiloff, and we explain why this is so. To connect the laboratory measurements to practical radiometer calibration, we present an example of a microwave radiometer calibration experiment exhibiting both standing wave and bath temperature drift effects and compare this with the expected relation between temperature drift and boiloff. We conclude in section 4 with suggestions for controlling errors due to the temperature drift effects described in this paper when performing field calibrations using LN2.

## 2. Liquid–vapor coexistence in $N_2$ – $O_2$ mixtures

The equilibrium state of a binary system such as an  $N_2$ – $O_2$  mixture is defined by three state variables, typically pressure  $P$ , temperature  $T$ , and  $O_2$  mole fraction  $x_{O_2}$ . For the  $N_2$ – $O_2$  system, the relationship between these state variables over the range of pressures typically encountered in radiometer calibrations is shown in the phase diagram in Fig. 1a, which has been computed from the data of Dodge and Dunbar (1927). In this diagram, a region of phase separation bounded by two intersecting boundary surfaces divides the liquid and vapor phases. The edges of the phase separation region, which lie in

the two planes defined by  $x_{\text{O}_2} = 0$  and  $x_{\text{O}_2} = 1$ , are the liquid–vapor coexistence curves for pure  $\text{N}_2$  and pure  $\text{O}_2$ , respectively. States in the interior of the phase separation region are unstable, and will divide into a mixture of corresponding homogeneous vapor and liquid phases having the same pressure and temperature, but different composition  $x_{\text{O}_2}$ .

At constant pressure, the phase diagram becomes the cross section in the  $T - x_{\text{O}_2}$  plane shown in Fig. 1b. Here, the upper boundary of the phase separation region is referred to as the condensation curve and the lower boundary as the boiling point curve. Homogeneous vapor and liquid phases in contact and in thermal equilibrium occupy corresponding states, such as those at points c and b having the same temperature but different composition. An unstable state such as point a will divide along an isotherm into homogeneous vapor and liquid phases at c and b, in proportions that conserve the total mass of  $\text{N}_2$  and  $\text{O}_2$  in the system.

The possible states of an open liquid bath are approximated by the constant pressure phase diagram in Fig. 1, provided that the temperature and composition of the gas in immediate contact with the liquid surface are not disturbed by advection. This may be the case, for example, in a deep container in calm air. Under these conditions, the temperature of the liquid bath will be close to the point on the boiling point curve corresponding to its composition  $x_{\text{O}_2}$ . However, even under this quasi-equilibrium condition, the composition of an open bath will not be stable over time unless  $x_{\text{O}_2} = 0$  or  $x_{\text{O}_2} = 1$ . The reason is that for intermediate values of  $x_{\text{O}_2}$ , the  $\text{O}_2$  mole fraction of the vapor leaving the system will always be lower than that of the liquid, so the  $\text{O}_2$  mole fraction of the liquid must increase as it boils away. Consequently, in calm conditions, the boiling point temperature of a pure LN2 bath is stable, but the boiling point temperature of a bath that has become contaminated with  $\text{O}_2$  will gradually rise toward the pure  $\text{O}_2$  boiling point.

The presence of advection that affects the temperature or composition of the gas in contact with the upper surface of the bath takes the system still further from equilibrium than the undisturbed case. The bath temperature will still tend to be driven toward the equilibrium boiling point via the formation of internal bubbles in the liquid, but larger shifts in the bath temperature from the equilibrium boiling point temperature can be expected. Some evidence of this is present in the measurements presented below.

### 3. Measurements

To make a quantitative assessment of the effect of  $\text{O}_2$  contamination on the boiling point temperature of an



FIG. 2. Laboratory test setup. Airflow was from right to left with the fans running. Air speeds were measured at points along the long edge of the container farthest from the fans.

LN2 bath under realistic conditions, we used the simple measurement setup shown in Fig. 2. The LN2 bath was held in an insulated container having a capacity of 3.3 L when filled to a depth of 100 mm. The liquid level in the bath was measured visually to approximately 1-mm accuracy using a wooden scale attached to one side of the container. Thermal contraction of this scale was verified to be negligible at the bath temperature. The container cross section was essentially constant, so that the bath volume was accurately proportional to depth.

The bath temperature was monitored by a Lake Shore Cryotronics model 211 temperature monitor and a DT-470 silicon diode temperature sensor at the bottom of the container. A calibration correction factor for the sensor's standard factory calibration curve was derived from a two-point calibration using the LN2 boiling point and a room temperature reference. The LN2 calibration point temperature was determined using the  $\text{N}_2$  vapor pressure data of Span et al. (2000), and the ambient pressure as measured with an Oaktron aneroid barometer. [We note that within their 0.1-K estimated error, the data of Dodge and Dunbar (1927) cited above for the  $\text{N}_2$ – $\text{O}_2$  system are in agreement with Span et al. (2000) for pure  $\text{N}_2$ .] The room temperature calibration point was obtained by comparison with a thermistor-based sensor (Digi-Sense model 400) calibrated to 0.03 K. With this two-point correction, the expected calibration error of the diode sensor is 0.1 K over the temperature range 70–300 K (Dodrill et al. 1991).

A pair of 90-mm square fans was used to produce an adjustable airflow across the top of the bath. Air speed across the container was measured using a Kestrel model 3000 handheld weather meter along the downstream edge of the container. At a given fan setting, the

ratio of maximum to minimum air speed  $v$  across the container was  $v_{\max}/v_{\min} \approx 1.5$ . Defining a midrange air speed as  $v_m = (v_{\max} + v_{\min})/2$ , tests were run for  $v_m$  ranging from  $v_m = 0.5 \text{ m s}^{-1}$  to  $v_m = 3.6 \text{ m s}^{-1}$  and in still air ( $v_m = 0$ ).

Liquid nitrogen was supplied as grade 4.8 (99.998%  $\text{N}_2$  by volume), containing less than 10 ppm  $\text{O}_2$ .

#### a. Effect of varying simulated wind speed

Field calibrations take place under a wide range of wind conditions. To study the effect of wind speed on the bath contamination rate, a series of runs was carried out during which the bath was filled with pure LN2 and allowed to settle to an initial depth  $h_0$  ranging from 96 to 100 mm. At this point, the fans were switched on and the bath was boiled completely away under the influence of constant wind speeds from  $v_m = 0$  to  $v_m = 3.6 \text{ m s}^{-1}$ . The bath temperature was logged continuously as a function of time  $t$  with a resolution of 1 s. To relate time and boiloff fraction, the depth  $h$  was noted visually on the depth scale and logged manually at irregular intervals. Once the bath was boiled completely away, the fans were switched off and a warm-up curve was recorded under calm conditions.

The results of these runs are compared in Fig. 3, in which normalized bath depth  $h/h_0$  and temperature  $T$  are plotted versus normalized time  $t/t_{1/2}$ , where  $t_{1/2}$  is the time at which half the bath had boiled away during each run. This normalization of the time axis facilitates a comparison across the wide range of boiloff times and best displays the variation of temperature with fractional change in volume discussed below.

Figure 3a shows that for all four runs, the boiloff rate remained constant in each case until the bath was nearly exhausted, so that the normalized measured depths  $h/h_0$  lie along a line  $h/h_0 = 1 - (1/2)(t/t_{1/2})$ . The temperature histories plotted in Fig. 3b show two important features. First, the case  $v_m = 0$  has a nearly constant boiloff temperature, whereas the three cases with simulated wind all display an upward temperature drift. Second, the three nonzero wind cases, which have a wide range of boiloff rates, have remarkably similar temperature histories as a function of  $t/t_{1/2}$ , especially for times  $t < t_{1/2}$ .

The  $v_m = 0$  case represents the familiar case of an LN2 bath in a calm laboratory environment. The bath, protected by an overlying layer of pure  $\text{N}_2$  boiloff gas, maintains a stable composition and temperature up to the point at which the liquid is exhausted. The behavior of the simulated wind cases can be understood as follows. We assume that the bath temperature corresponds closely to the  $\text{O}_2$  mole fraction along the  $\text{N}_2$ – $\text{O}_2$  boiling point curve, so that the similar temperature histories indicate similar  $\text{O}_2$  mole fraction histories, despite the

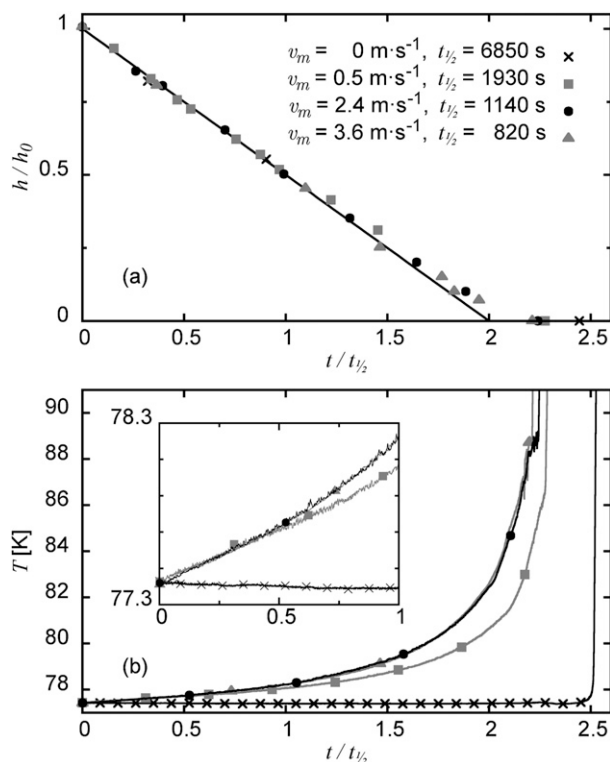


FIG. 3. Boiloff of an initially pure LN2 bath under varying simulated wind speeds. Normalized (a) bath depth  $h/h_0$  and (b) temperature  $T$  are plotted vs normalized time  $t/t_{1/2}$ , where  $t_{1/2}$  is the time for one-half of the bath to boil away. The solid line in (a) is the ideal constant rate boiloff curve,  $h/h_0 = 1 - (1/2)(t/t_{1/2})$ . In (b), symbols are plotted at 600-s intervals.

different advective heat loads. We further assume that the advective heat load is the dominant heat load on the bath. Under this assumption, the volume of gas evolved from the bath will depend only upon the volume of warm advecting gas that condenses into the bath (the evolved gas volume will be greater because the heat load of the condensed gas includes both its latent heat and its cooling from ambient temperature). At constant pressure, the difference in  $\text{O}_2$  mole fraction between the condensing gas and the evolving gas, which determines the net  $\text{O}_2$  accumulated per volume of gas evolved, can only depend on the bath temperature and  $\text{O}_2$  mole fraction, which track one another along the boiling point curve. Normalizing to total volume, this implies that a given fractional change in bath volume will be accompanied by a change in  $\text{O}_2$  mole fraction that depends on the current bath temperature. In summary, for a bath subjected to a dominating advective heat load from gas at constant composition and temperature, starting from a given initial condition (such as pure LN2), the subsequent temperature and  $\text{O}_2$  mole fraction will be functions of the fractional change in bath volume only, and not of the boiloff rate or the bath volume itself.

The inset in Fig. 3b shows that for the first 25% of change in bath volume, the temperature change of a bath consisting initially of pure LN2 is nearly linear in the fractional volume change  $\Delta V/V_0$ , such that

$$\Delta T = a \frac{\Delta V}{V_0}, \quad (1)$$

where  $a = -1.2(1) \text{ K}$ ; that is, the initial rise in bath temperature is about 12 mK for every 1% of the initial volume  $V_0$  that has boiled away. The estimated uncertainty in the coefficient  $a$  reflects the spread in the values observed across these runs.

### b. Effect of repeated refills

Often, an LN2 calibration target is refilled several times in the course of a calibration run to make up for liquid boiloff. We carried out a series of runs to investigate the behavior of a bath given a number of successive refills. In these runs, the bath was filled to an initial depth  $h_0$ , either  $h_0 = 100 \text{ mm}$  or  $h_0 = 60 \text{ mm}$ , then subjected to a  $v_m = 3.6 \text{ m s}^{-1}$  simulated wind. When the bath depth  $h$  fell to  $h = f h_0$ , where the volume fraction  $f$  was either  $f = 0.5$  or  $f = 0.8$ , the fans were stopped to permit a stable temperature reading under quasi-equilibrium conditions, then the bath was refilled to  $h_0$ . After an additional short delay to observe the temperature, the fans were restarted. This cycle was repeated until the system reached a steady-state temperature cycle. The results of these runs, shown in Fig. 4, confirm that the bath temperature history follows the fractional volume change history as discussed above, and they demonstrate how the steady-state bath temperature cycle depends on the volume fraction  $f$  at which the load is refilled.

For the run plotted in Fig. 4a,  $h_0 = 100 \text{ mm}$  and  $f = 0.5$ . The lettered points on the temperature curve correspond to the similarly lettered points on the boiling point curve in Fig. 4d, computed for  $P = 1028 \text{ mbar}$ , the ambient pressure at the time of this run. Starting as pure LN2 with  $h_0 = 100 \text{ mm}$  at A, the system evolves along the boiling point curve to B, where the depth has decreased to  $h = 50 \text{ mm}$ . At this point, the bath is refilled to depth  $h_0$  with pure LN2, diluting the  $\text{O}_2$  mole fraction by a factor  $f$  to point C. A similar cycle occurs on boiling from C to D and on refilling from D to E. Eventually, the system reaches a steady state between points such as F and G when the increase in  $\text{O}_2$  mole fraction during boiloff matches the decrease in  $\text{O}_2$  mole fraction from dilution with pure LN2 during refills.

The run in Fig. 4b is similar to that in Fig. 4a, with  $f = 0.5$ , but in this case  $h_0 = 60 \text{ mm}$ . The evolution of  $T$  over the successive fractional bath volume changes is similar,

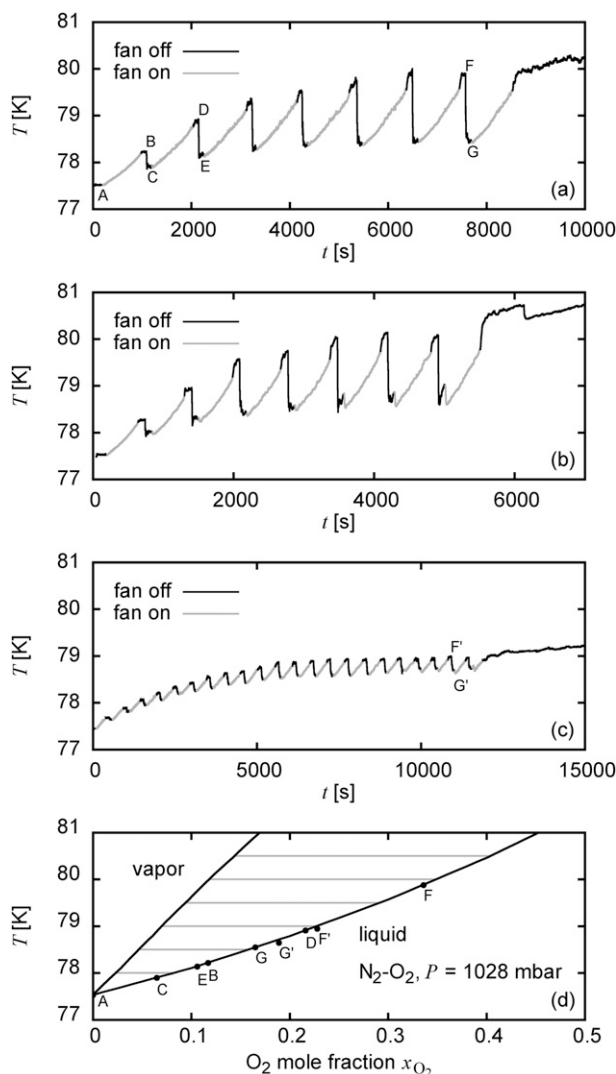


FIG. 4. Temperature histories for a bath successively refilled with pure LN2, subjected to  $v_m = 3.6 \text{ m s}^{-1}$  simulated wind speed. During refills, the fan was switched off (darker trace) to facilitate stable temperature and level readings. (a) The bath was initially filled with LN2 to a depth of 100 mm, and refilled to 100 mm after falling to a depth of 50 mm. (b) Initially filled to 60 mm, and refilled to 60 mm from 30 mm. (c) Initially filled to 100 mm, and refilled to 100 mm from 80 mm. In (d), the temperatures at the labeled points in (a) and (c) are located along the  $\text{N}_2\text{-O}_2$  boiling point curve. The steady-state  $\text{O}_2$  mole fractions at F and G in (a) and at F' and G' in (c) have the expected approximate ratios 100:50 and 100:80, respectively.

but it occurs on a faster time scale because of the smaller bath volume. This run exhibited more temperature instability than the run in Fig. 4a, particularly immediately after refills. We attribute this to less efficient mixing in the shallower bath.

For the run plotted in Fig. 4c, the bath was initially filled to a depth  $h_0 = 100 \text{ mm}$  as in Fig. 4a, but refills

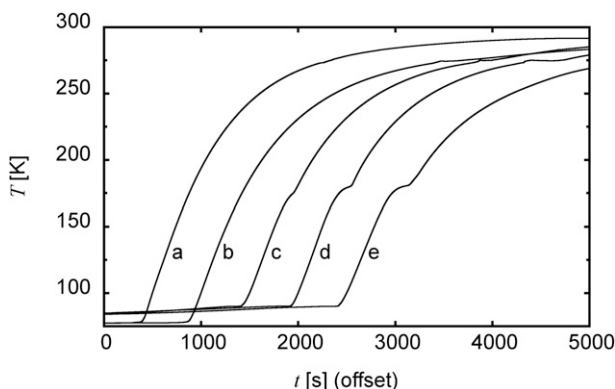


FIG. 5. Warming curves. Curve a is a dry reference curve obtained after cooling the bath container with a small amount of LN<sub>2</sub>. Curves b–e follow runs with significant water ice accumulation; these show comparatively slower warming and a melting feature at 273 K. Curve b follows the run in Fig. 3 with  $v_m = 0$  and no O<sub>2</sub> accumulation. Curves c, d, and e were recorded under still conditions following the runs in Figs. 4b, 4a, and 4c, respectively, with  $v_m = 3.6 \text{ m s}^{-1}$  and with accumulated O<sub>2</sub>. These display an endothermic feature starting near  $T = 175 \text{ K}$  as amorphous ice desorbs trapped gas and crystallizes.

were made when the bath volume had been reduced by a factor  $f = 0.8$ , or  $h = 80 \text{ mm}$ . The ratio of the O<sub>2</sub> mole fraction at the extremes F' and G' of the steady-state cycle is likewise 0.8, and the temperature swing is correspondingly smaller than for the cases with  $f = 0.5$  above.

### c. Ice accumulation and warming curves

During boiloff runs, the bath typically accumulated a few grams of water ice at the bottom of the container. Differences in the properties of the accumulated ice were noted depending on whether it was accumulated under calm or simulated wind conditions. These differences are noteworthy in view of active interest in the properties of glassy and crystalline water (Angell 2008; Sepúlveda et al. 2012), and crystallization-induced desorption of impurities trapped in amorphous solid water (Smith et al. 1997; May et al. 2013). Moreover, they provide further evidence of the different nature of the contact between the bath and environmental air under calm versus windy conditions.

In Fig. 5, warming curves are plotted for the container returning to ambient temperature in still air following five runs. All were acquired at similar ambient temperature ranging from 21.5° to 23.5°C, and relative humidity ranging from 27% to 56%. Curve a is a dry reference curve obtained after cooling the bath container with a small amount of LN<sub>2</sub>. Curves b–e follow runs with significant ice accumulation. These show slower warming due to sublimation, evaporation, and the added heat

capacity of the accumulated water, as well as a melting feature at 273 K.

Curve b follows the run in Fig. 3 with  $v_m = 0$ . No O<sub>2</sub> accumulated in the bath during this run, so the final boiling temperature before warming commenced was the pure LN<sub>2</sub> boiling point  $T = 77.3 \text{ K}$ . The N<sub>2</sub> gas blanket that prevented O<sub>2</sub> uptake would also have prevented water vapor from reaching the liquid surface. Thus, the accumulated ice in the bath must have formed initially as liquid droplets or ice grains in the fog lying above the N<sub>2</sub> blanket, and precipitated under gravity into the bath as grains of ice. The ice in this case will have formed relatively slowly, at a temperature at or above the homogeneous nucleation point,  $T \sim 235 \text{ K}$ , as crystalline ice  $I_h$ .

Curves c, d, and e were recorded under still conditions following the runs in Figs. 4b, 4a, and 4c, respectively, with  $v_m = 3.6 \text{ m s}^{-1}$ . Because O<sub>2</sub> accumulated in the bath, the final boiling temperature before the bath was exhausted was near the pure O<sub>2</sub> boiling point,  $T = 90 \text{ K}$ . During these runs, ambient water vapor would have been brought quickly into direct contact with the bath surface. The resulting rapid quenching can produce glassy or amorphous solid water, with the possible incorporation of O<sub>2</sub> or N<sub>2</sub> as impurities. The endothermic feature in these curves at  $T \sim 175 \text{ K}$  is evidence for this. For amorphous water films formed by vapor deposition below 150 K, Sepúlveda et al. (2012) observed a weak endothermic signature of a glass transition starting at 174 K, followed by (exothermic) crystallization near 200 K. The energy scale of the feature observed here, which is roughly comparable to the latent heat of melting at 273 K, is too large to be accounted for directly by these processes. Instead, it appears that the visible feature is due to desorption of incorporated O<sub>2</sub> or N<sub>2</sub>, induced by the glass transition or subsequent crystallization in a process akin to that described by May et al. (2013). Qualitatively, we observed the width of the feature to increase with increasing exposure time to advecting air and increased relative humidity.

### d. Radiometer calibration example

As an illustration of the effects described in this paper under practical conditions, we present a measurement from a series obtained in a meteorological radiometer calibration experiment (Küchler 2012). In these measurements, the radiometric brightness temperature of an LN<sub>2</sub> calibration target was monitored for extended periods to study standing wave and drift effects. The radiometer was a Humidity and Temperature Profiler (HATPRO) produced by Radiometer Physics GmbH (Rose et al. 2005), operating in its normal outdoor environment.

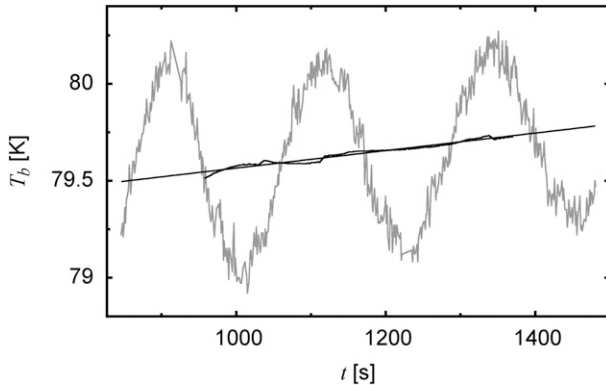


FIG. 6. Calibrated  $T_b$  (gray) in the 23.04-GHz channel of a meteorological radiometer viewing an LN2 calibration load over a 10-min period. A 222-s rectangular moving time average and regression line are shown in black. The sinusoidal variation in  $T_b$  is due to standing wave interference between internal reflections in the radiometer and the LN2 surface; each cycle corresponds to a half-wavelength change in the height of the LN2 surface as the bath boils away. The moving average tracks the change in bath temperature as it accumulates  $O_2$ .

In the measurement shown in Fig. 6, the radiometer beam was directed via a reflector at a calibration target consisting of a convoluted foam microwave absorber submerged in an LN2 bath, at normal incidence to the bath surface. This plot shows the brightness temperature  $T_b$  observed at 1-s intervals for the 23.04-GHz channel, as a function of time since the initial filling of the calibration target with LN2. The period plotted here follows the first topping up of the bath after the initial refilling. During this measurement, the radiometer and calibration targets were protected from direct wind gusts by a sheet. Nevertheless, formation of a pure  $N_2$  gas layer over the LN2 surface was prevented by residual air movement and by the action of the HATPRO's dew blower fan, which remains on during calibration to prevent condensation on the radiometer's radome. The brightness temperature  $T_b$  was derived from a prior calibration of the radiometer using the same target and the vendor-supplied software, which includes a correction for an ambient-terminated power reflection from the LN2 surface but does not account for coherent interference. For the temperature drift rate measurement discussed below, the temperature offset error in this calibration is not important, and the gain calibration accuracy is more than adequate.

The normal incidence to the target results in standing wave interference between the reflection from the LN2 bath surface and internal reflections in the radiometer. This interference produces a calibration offset that varies sinusoidally as the level of the LN2 bath surface changes. Each cycle in  $T_b$  plotted in Fig. 6 corresponds to a half-wavelength change in LN2 surface height, where  $\lambda/2 = 6.51$  mm.

In addition to the standing wave pattern, the  $T_b$  measurement in Fig. 6 exhibits a drift due to  $O_2$  contamination. By performing a rectangular moving average over the standing wave period, the drift can be isolated as shown by the black curve in Fig. 6. The standing wave period,  $t_s = 222$  s, was determined by iterating over the averaging period to find the best linear fit. The drift rate, from the fitted regression slope, is

$$\frac{dT_b}{dt} = 0.45(1) \text{ mK s}^{-1}. \quad (2)$$

This result can be compared with the bath temperature drift rate predicted by Eq. (1) as follows. The rate of change of the bath depth is found from the standing wave period, and is

$$\frac{dh}{dt} = \frac{\lambda}{2t_s} = 2.93 \times 10^{-2} \text{ mm s}^{-1}. \quad (3)$$

To find the initial depth  $h_0$  we assume the target container, which is 100 mm deep, was initially filled with LN2 to 95(5)-mm depth. This must be corrected for the displacement of the foam absorber and a 5-mm-thick solid panel to which it is mounted. The foam absorber is 73 mm thick but consists mostly of empty space; its effective displacement thickness was measured as 11.5 mm by immersing a sample of the material in water and dividing the displaced water volume by the absorber area. Accounting for these corrections,  $h_0 = 79(5)$  mm, and the fractional rate of change of the bath volume is

$$\frac{d \Delta V}{dt V_0} = \frac{1}{h_0} \frac{dh}{dt} = 3.7(2) \times 10^{-4} \text{ s}^{-1}. \quad (4)$$

From Eq. (1), the predicted drift rate in the bath temperature is

$$\frac{d}{dt} \Delta T = a \left( \frac{d \Delta V}{dt V_0} \right) = 0.44(5) \text{ mK s}^{-1}, \quad (5)$$

which is in good agreement with the measured brightness temperature drift rate, Eq. (2).

The simple procedure we used here to extract the drift rate works well when, as in this example, the boiloff rate is approximately constant and the advective heat load at the bath surface dominates the heat load. Not all calibration runs are amenable to this simple analysis. Nevertheless, the coupling between the time evolution of the standing wave and the drift in bath temperature suggests that a calibration algorithm can be devised that simultaneously corrects for standing wave interference and target temperature drift, using data collected over two

or more standing wave cycles. A general algorithm would need to handle the case of a nonuniform boiloff rate, and it would need to account for the fixed contribution to the boiloff rate of the conductive heat load into the bath. It would also require a standing wave effect that varies with the distance to the LN<sub>2</sub> surface. This will typically be present when the target is viewed from above at near-normal incidence. We are currently collecting additional data to support development of a correction procedure; this will be the subject of a future paper.

#### 4. Concluding remarks

An absorbing target cooled with liquid nitrogen is widely used as an absolute radiometric calibration standard for meteorological radiometers operated outdoors. However, a liquid nitrogen bath in a typical outdoor environment with even mild air movement will exhibit an upward drift in boiling point temperature as it becomes contaminated with O<sub>2</sub> from the surrounding air. We have shown that under typical conditions, initial boiling point drift rates of order 25 mK min<sup>-1</sup> can occur, and that the steady-state boiling point of a bath maintained by regular additions of LN<sub>2</sub> can eventually increase by approximately 2 K. This is in striking contrast to the highly stable temperature normally observed for a liquid nitrogen bath in calm laboratory conditions. We have demonstrated the effect under a range of simulated wind conditions in the laboratory and in a field measurement with a meteorological radiometer, and explained in detail the physical processes involved.

A key finding from this study is that for a bath initially consisting of pure LN<sub>2</sub>, under conditions where advective heat transfer from atmospheric air at the liquid surface is the dominant heat load, the boiling point increase is a predictable function [Eq. (1)] of the fractional change in bath volume, independent of the boiloff rate. To the extent that other heat loads become important, such as may occur during periods of calm air, the predicted temperature rise can be taken as an upper bound.

Given a desired calibration accuracy, Eq. (1) can be used to set a limit on the fraction of the initial pure LN<sub>2</sub> fill that can be allowed to boil away before a calibration is completed. This limit can simply be indicated by a fiducial mark or a scale on the bath container and monitored visually. Measures to reduce the boiloff rate, such as a wind shield, would increase the available time for calibration.

Other mitigation strategies are possible. A transparent cover can be used to prevent contact with ambient air, but this introduces into the calibration path a potentially lossy or reflective element upon which water can condense. Alternatively, the temperature of the bath can simply be

monitored with a temperature sensor as in the present paper. For the differential changes in bath temperature that are important here the calibration requirements on this sensor are modest: the initial reading when the bath is first filled provides a pure LN<sub>2</sub> boiling point reference, from which the changes need only be measured to an accuracy of a few percent.

In addition to the temperature drift, which is the main focus of this paper, reflections from the LN<sub>2</sub> bath surface that produce a standing wave between the radiometer and calibration target must also be accounted for or otherwise mitigated to achieve absolute radiometric accuracy. Observing a full cycle or more of the standing wave as the LN<sub>2</sub> boils away is one way to do this. We have shown that the standing wave can be simultaneously exploited to monitor the change in bath volume with time, which can be related to the temperature drift of the bath. We are currently working on development of a practical calibration correction algorithm accounting for both effects, which will be the subject of a future paper.

*Acknowledgments.* We thank Drs. Susanne Crewell, Ulrich Löhnert, Gerrit Maschwitz, and Thomas Rose for helpful discussions regarding this work, and R. Haseneder-Lind for assistance with the field experiments. This study was partly funded by the TransRegio32 project, which also provided travel support for DDT to visit the University of Cologne.

#### REFERENCES

- Angell, C. A., 2008: Insights into phases of liquid water from study of its unusual glass-forming properties. *Science*, **319**, 582–587, doi:10.1126/science.1131939.
- Dodge, B. F., and A. K. Dunbar, 1927: An investigation of the coexisting liquid and vapor phases of solutions of oxygen and nitrogen. *J. Amer. Chem. Soc.*, **49**, 591–610, doi:10.1021/ja01402a002.
- Dodrill, B. C., J. K. Krause, P. R. Swinehart, and V. Wang, 1991: Performance characteristics of silicon diode cryogenic temperature sensors. *Applications of Cryogenic Technology*, J. P. Kelley, Ed., Vol. 10, Plenum Press, 85–106.
- Hardy, W. N., 1973: Precision temperature reference for microwave radiometry. *IEEE Trans. Microwave Theory Tech.*, **21**, 149–150, doi:10.1109/TMTT.1973.1127954.
- Küchler, N., 2012: Kalibration von Mikrowellenradiometern. Bachelorarbeit, Institut für Geophysik und Meteorologie, Universität zu Köln, 61 pp.
- May, R. A., R. S. Smith, and B. D. Kay, 2013: The release of trapped gases from amorphous solid water films. I. “Top-down” crystallization-induced crack propagation probed using the molecular volcano. *J. Chem. Phys.*, **138**, 104501, doi:10.1063/1.4793311.
- Paine, S. N., and D. D. Turner, 2013: Processing and calibration of submillimeter Fourier transform radiometer spectra from the RHUBC-II campaign. *IEEE Trans. Geosci. Remote Sens.*, **51**, 5187–5198, doi:10.1109/TGRS.2012.2231869.

- Penzias, A. A., and C. A. Burrus, 1973: Millimeter-wavelength radio-astronomy techniques. *Annu. Rev. Astron. Astrophys.*, **11**, 51–72, doi:10.1146/annurev.aa.11.090173.000411.
- Pospichal, B., G. Maschwitz, N. Küchler, and T. Rose, 2012: Standing wave patterns at liquid nitrogen calibration of microwave radiometers. *Proc. Ninth Int. Symp. on Tropospheric Profiling*, L'Aquila, Italy, European Space Agency, P35. [Available online at [http://meteorema.aquila.infn.it/istp/proceedings/Session\\_P\\_Posters/P35\\_Pospichal.pdf](http://meteorema.aquila.infn.it/istp/proceedings/Session_P_Posters/P35_Pospichal.pdf).]
- Randa, J., D. K. Walker, A. E. Cox, and R. L. Billinger, 2005: Errors resulting from the reflectivity of calibration targets. *IEEE Trans. Geosci. Remote Sens.*, **43**, 50–58, doi:10.1109/TGRS.2004.839809.
- Rose, T., S. Crewell, U. Löhnert, and C. Simmer, 2005: A network suitable microwave radiometer for operational monitoring of the cloudy atmosphere. *Atmos. Res.*, **75**, 183–200, doi:10.1016/j.atmosres.2004.12.005.
- Sepúlveda, A., E. Leon-Gutierrez, M. Gonzalez-Silveira, C. Rodríguez-Tinoco, M. T. Clavaguera-Mora, and J. Rodríguez-Viejo, 2012: Glass transition in ultrathin films of amorphous solid water. *J. Chem. Phys.*, **137**, 244506, doi:10.1063/1.4771964.
- Smith, R. S., C. Huang, E. K. L. Wang, and B. D. Kay, 1997: The molecular volcano: Abrupt CCl<sub>4</sub> desorption driven by the crystallization of amorphous solid water. *Phys. Rev. Lett.*, **79**, 909–912, doi:10.1103/PhysRevLett.79.909.
- Span, R., E. W. Lemmon, R. T. Jacobsen, W. Wagner, and A. Yokozeki, 2000: A reference equation of state for the thermodynamic properties of nitrogen for temperatures from 63.151 to 1000 K and pressures to 2200 MPa. *J. Phys. Chem. Ref. Data*, **29**, 1361–1433, doi:10.1063/1.1349047.